



## Article

# Novel MOF shell-derived surface modification of Li-rich layered oxide cathode for enhanced lithium storage

Zhitong Xiao<sup>a</sup>, Jiashen Meng<sup>a</sup>, Qi Li<sup>a</sup>, Xuanpeng Wang<sup>a</sup>, Meng Huang<sup>a</sup>, Ziang Liu<sup>a</sup>, Chunhua Han<sup>a,\*</sup>, Liqiang Mai<sup>a,b,\*</sup>

<sup>a</sup>State Key Laboratory of Advanced Technology for Materials Synthesis and Processing, International School of Materials Science and Engineering, Wuhan University of Technology, Wuhan 430070, China

<sup>b</sup>Department of Chemistry, University of California, Berkeley, CA 94720, USA

## ARTICLE INFO

## Article history:

Received 12 September 2017

Received in revised form 30 November 2017

Accepted 11 December 2017

Available online 13 December 2017

## Keywords:

Surface modification

MOF shell

Li-rich layered oxide

Lithium-ion battery

## ABSTRACT

Li-rich layered oxide materials have attracted increasing attention because of their high specific capacity (>250 mAh g<sup>-1</sup>). However, these materials typically suffer from poor cycling stability and low rate performance. Herein, we propose a facile and novel metal-organic-framework (MOF) shell-derived surface modification strategy to construct NiCo nanodots decorated (~5 nm in diameter) carbon-confined Li<sub>1.2</sub>Mn<sub>0.54</sub>Ni<sub>0.13</sub>Co<sub>0.13</sub>O<sub>2</sub> nanoparticles (LLO@C&NiCo). The MOF shell is firstly formed on the surface of as-prepared Li<sub>1.2</sub>Mn<sub>0.54</sub>Ni<sub>0.13</sub>Co<sub>0.13</sub>O<sub>2</sub> nanoparticles via low-pressure vapor superassembly and then is *in situ* converted to the NiCo nanodots decorated carbon shell after subsequent controlled pyrolysis. The obtained LLO@C&NiCo cathode exhibits enhanced cycling and rate capability with a capacity retention of 95% after 100 cycles at 0.4 C and a high capacity of 159 mAh g<sup>-1</sup> at 5 C, respectively, compared with those of LLO (75% and 105 mAh g<sup>-1</sup>). The electrochemical impedance spectroscopy and selected area electron diffraction analyses after cycling demonstrate that the thin C&NiCo shell can endow LLO with high electronic conductivity and structural stability, indicating the undesired formation of the spinel phase initiated from the particle surface is efficiently suppressed. Therefore, this presented strategy may open a new avenue on the design of high-performance electrode materials for energy storage.

© 2017 Science China Press. Published by Elsevier B.V. and Science China Press. All rights reserved.

## 1. Introduction

Rapid development of portable electronics and electric vehicles requires lithium-ion batteries (LIBs) to have high energy/power density, low cost, good safety and long lifespan [1–4]. In a commercial LIB, the traditional cathode and anode materials are LiCoO<sub>2</sub> and graphite, respectively. Compared with the commercial graphite (theoretical capacity 372 mAh g<sup>-1</sup> [5]), the LiCoO<sub>2</sub> has a low specific capacity of 150 mAh g<sup>-1</sup> [6] which becomes a big bottleneck of the battery breakthroughs. Among numerous cathode materials, Li-rich layered oxide (LLO) materials,  $x\text{Li}_2\text{MnO}_3\cdot(1-x)\text{LiMO}_2$  (M = Ni, Co, Mn, etc.), have attracted increasing attention as promising candidates because of their high specific capacity (>250 mAh g<sup>-1</sup>), high operating voltage (>3.5 V vs. Li<sup>+</sup>/Li), low cost and low toxicity [7–10]. The available capacity and voltage variation for the typical lithium-containing cathode materials are summarized in Fig. S1 (online). It is noted that the energy density of LLO is

900–1100 Wh kg<sup>-1</sup> which is higher than that of traditional cathode materials, such as LiCoO<sub>2</sub> (about 550 Wh kg<sup>-1</sup>) and LiMn<sub>2</sub>O<sub>4</sub> (about 450 Wh kg<sup>-1</sup>). However, LLO typically suffers from large irreversible capacity loss in the initial cycle, low first-cycle Columbic efficiency, poor cycling stability and low rate performance, which hinder its further applications in real portable electronics and emerging electrical/hybrid vehicles [11–18].

In the past decade, researchers have investigated the irreversible oxygen loss at the surface and/or O<sup>-</sup> formation in the lattice, which led to high charging capacity and significant irreversible capacity loss in the first cycle [19–22]. Moreover, an undesired spinel growth in the layered host structure usually occurred from the surface during the long-term cycling, which led to the fast capacity fading and voltage decaying [23–26]. One efficient and simple method to solve the aforementioned problems and improve the electrochemical performance is via doping elements in crystal lattices of LLO by ions, such as Mg<sup>2+</sup> [13], Al<sup>3+</sup> [27], F<sup>-</sup> [28] and (BO<sub>3</sub>)<sup>3-</sup> [29], to supersede transition metal or lithium ions. Another efficient approach is surface modification of LLO by coating a thin layer of protective materials, including AlF<sub>3</sub> [30], Al<sub>2</sub>O<sub>3</sub> [31], AlPO<sub>4</sub> [32], Li<sub>2</sub>ZrO<sub>3</sub> [33], LiCoPO<sub>4</sub> [34] and

\* Corresponding authors.

E-mail addresses: hch5927@whut.edu.cn (C. Han), mlq518@whut.edu.cn (L. Mai).

$\text{LiFePO}_4$  [35]. For instance, Zheng et al. [35] designed a surface modification with  $\text{LiFePO}_4$ , which provides lithium ion and charge transport channels as well as protects the surface structure from side reactions at the electrode/electrolyte interface. Moreover, surface modification via carbon coating has been widely applied to cathode materials (e.g.,  $\text{LiFePO}_4$  [36],  $\text{Li}_2\text{MnO}_4$  [37], and  $\text{LiNi}_{1/3}\text{Mn}_{1/3}\text{Co}_{1/3}\text{O}_2$  [38]) to provide enhanced structure stability and high electronic conductivity, thereby improving the rate capability and cycling performance [39]. However, this carbon coating strategy is rarely applied to modify LLO.

Herein, we developed a facile and novel surface modification strategy to synthesize NiCo nanodots decorated carbon-confined LLO nanoparticles. In detail, a thin MOF shell was first generated on LLO nanoparticles by low-pressure vapor superassembly, and then after *in situ* carbonization, the obtained MOF shell was converted to the C&NiCo shell. This method is a high-yield, low-cost and simple-manipulation method, which can be used to coat a uniform carbon shell on various substrates [40]. The as-synthesized heterostructured C&NiCo shell provides a stable structure and high electronic conductivity, and hence the obtained LLO@C&NiCo cathode exhibits enhanced electrochemical performance in LIBs.

## 2. Experimental

### 2.1. Synthesis of the LLO

All the reagents were of analytical grade and used without further purification.  $\text{Li}_{1.2}\text{Mn}_{0.54}\text{Ni}_{0.13}\text{Co}_{0.13}\text{O}_2$  was prepared using a sol-gel method.  $\text{LiCH}_3\text{COO}\cdot 2\text{H}_2\text{O}$ ,  $\text{Mn}(\text{CH}_3\text{COO})_2\cdot 4\text{H}_2\text{O}$ ,  $\text{Ni}(\text{CH}_3\text{COO})_2\cdot 4\text{H}_2\text{O}$ , and  $\text{Co}(\text{CH}_3\text{COO})_2\cdot 4\text{H}_2\text{O}$  with a stoichiometric ratio of 1.26:0.54:0.13:0.13 (Li 5% excess) were dissolved in 20 mL ethanol containing 2.5 g polyvinyl pyrrolidone (PVP). The mixture was stirred for 12 h at room temperature and then heated at 70 °C for overnight. The primary product was calcined at 900 °C for 10 h in air to obtain LLO black powder.

### 2.2. Synthesis of the LLO@C&NiCo

0.1 g as-prepared  $\text{Li}_{1.2}\text{Mn}_{0.54}\text{Ni}_{0.13}\text{Co}_{0.13}\text{O}_2$  powder and 0.5 g 2-methylimidazole were mixed uniformly. Then the mixture was heated at 150 °C for 8 h under low-pressure condition (~100 Pa). The resultant intermediate powder (LLO@MOF) was finally calcined in argon gas at 450 °C for 2 h to obtain the final product, black LLO@C&NiCo powder.

### 2.3. Materials characterization

X-ray diffraction (XRD) characterization was recorded with a D8 Discover X-ray diffractometer with non-monochromated Cu K $\alpha$  X-ray source ( $\lambda = 1.054056 \text{ \AA}$ ). Scanning electron microscopy (SEM) images were obtained using a JEOL JSM-7100F at an acceleration voltage of 20 kV. Transmission electron microscopy (TEM), high resolution TEM (HRTEM) and selected area electron diffraction (SAED) images were collected by a JEM-2100F/Titan G2 60–300 microscope. Elemental mapping was performed using an EDX-GENESIS 60S spectrometer. Thermogravimetric analysis (TGA) and differential scanning calorimeter (DSC) curves were conducted by using a Netzsch STA 449 C simultaneous analyzer. Raman spectrum was performed using a Renishaw INVIA micro-Raman spectroscopy system. X-ray photoelectron spectroscopy (XPS) measurements were obtained using a VG MultiLab 2000 instrument. Fourier transform-infrared (FT-IR) transmittance spectra were measured using a Nicolet 60-SXB IR spectrometer. The Brunauer-Emmett-Teller (BET) surface area was calculated from nitrogen adsorption isotherms collected at 77 K using a Tristar

3200 instrument. *In situ* XRD experiments during electrochemical measurement of batteries were performed on a D8 Discover X-ray diffractometer equipped with a non-monochromated Cu K $\alpha$  X-ray source; the prepared two materials *in situ* cells were charged to 4.8 V and then discharged to 2 V at 0.2 C, with  $2\theta$  recorded from 16° to 22°. Ampere-voltage curves ( $I$ - $V$  curves) were measured using a Lake shore PPT4 probe station and an Agilent B1500A semiconductor device analyzer. The LLO or LLO@C&NiCo powders were crushed to 2 mm × 2 mm × 1 mm sheet.

### 2.4. Electrochemical measurement

The as-synthesized LLO or LLO@C&NiCo powder was mixed with acetylene black and polyvinylidene fluoride (PVDF) in a weight ratio of 7:2:1 in N-methyl-2-pyrrolidone (NMP) to form a slurry. Then the slurry was coated onto Al foil and then dried at 70 °C for 12 h in a vacuum oven to obtain as-prepared cathodes. The electrochemical measurement was conducted with CR2016 coin-type half-cells assembled in an Ar-filled glove box. The half cells consisted of an as-prepared cathode, a Li metal anode, and LB-315 5 V high-voltage electrolyte. Galvanostatic charge/discharge measurements were performed using a multichannel battery testing system (LAND CT2001A). Cycling voltammetry (CV) and electrochemical impedance spectroscopy (EIS) were collected with an Autolab potentiostat/galvanostat.

## 3. Results and discussion

### 3.1. Morphology and structure characterization

The fabrication procedure of LLO@C&NiCo is schematically displayed in Fig. 1a. Initially, LLO nanoparticles are synthesized via a sol-gel method and followed by heat treatment in air. From the XRD pattern (Fig. 1b), the main peaks are well identified as hexagonal  $\alpha\text{-NaFeO}_2$  structured layered oxides with the  $R\bar{3}m$  space group. While the low intensity superlattice peaks in the range of 20–25° are attributed to the  $\text{Li}_2\text{MnO}_3$ -like component with a space group of  $C2/m$  [10,41–43]. SEM image shows that the particles have 100–500 nm in diameter (Figs. 1e and S2a online). The interstices between the particles vary from 100 to 600 nm, which can facilitate the low-pressure vapor superassembly process. The MOF shell is firstly formed on the surface of as-prepared LLO nanoparticles after low-pressure vapor superassembly (step I) to obtain LLO@MOF. At this stage, the MOF phase cannot be detected (Fig. 1c) via XRD because only a tiny amount and thin layer of MOF shell is coated on LLO. However, from FT-IR spectra (Fig. S3 online), the typical signal peaks at 700 to 1700  $\text{cm}^{-1}$  and 2929  $\text{cm}^{-1}$  originated from C=N stretch and aliphatic C–H stretch [44] are observed, suggesting the existence of thin MOF shell in LLO@MOF. Moreover, the LLO@MOF exhibits a relatively larger BET surface area of  $47 \text{ m}^2 \text{ g}^{-1}$  than that of LLO ( $1.9 \text{ m}^2 \text{ g}^{-1}$ ) (Fig. S4 online), suggesting the existence of thin MOF shell in LLO@MOF. The morphology of LLO@MOF is almost unchanged from LLO (Figs. 1f and S2b online). During the subsequent controlled pyrolysis (step II), the MOF shell is *in situ* converted into NiCo nanodots decorated carbon shell to obtain LLO@C&NiCo. The LLO@C&NiCo exhibits nearly identical XRD pattern as that of LLO (Fig. 1d) and the morphology of LLO@C&NiCo is well maintained (Figs. 1g and S2c online).

TEM images (Figs. 2a, b and S5 online) of LLO@C&NiCo show well-defined nanoparticles with many “dark spots” distributed on the surface. HRTEM image (Fig. 2c) clearly exhibits the continuous amorphous carbon shell with a uniform thickness of around 2 nm. The NiCo alloy nanodots with a diameter of around 5 nm are distributed in the derived carbon shell. The measured interlayer distance of 0.47 nm is in agreement with the (0 0 3) plane of the

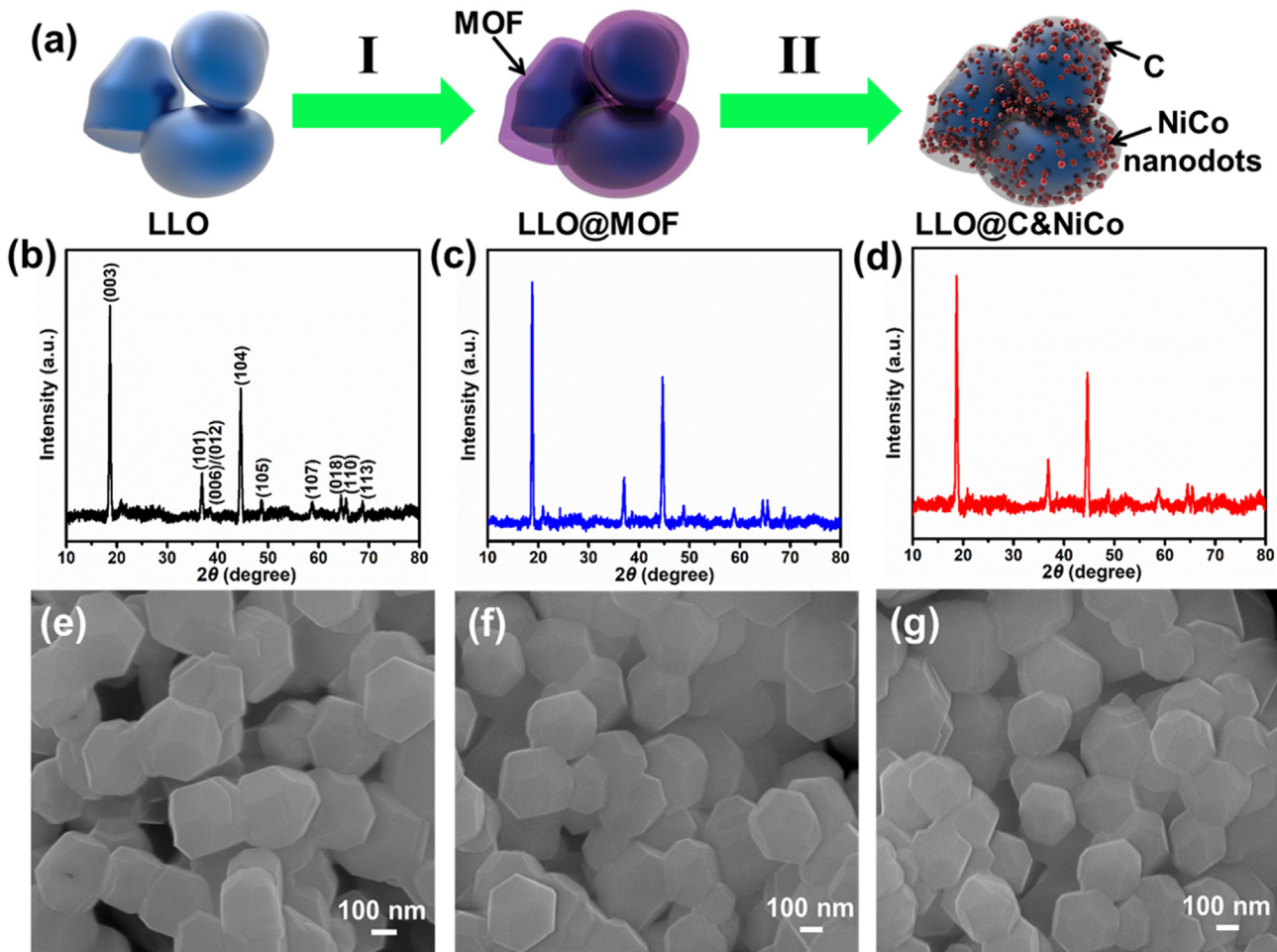


**Fig. 1.** (Color online) Synthesis procedure and characterizations of LLO@C&NiCo. (a) Schematic illustration of the formation procedure of LLO@C&NiCo. (b)–(d) XRD patterns and (e)–(g) SEM images of LLO, LLO@MOF and LLO@C&NiCo, respectively.

layered structure [35]. The corresponding SAED pattern (Fig. 2d) reveals hexagonal symmetry, which is typical for a  $\bar{R}\bar{3}m$  space group. Moreover, the extra diffraction spot is indexed to the (1 1 1) plane of the NiCo alloy [45], indicating the existence of NiCo alloy. The HRTEM and TEM mapping images of LLO are presented in Fig. S6 (online).

According to the TGA results (Fig. 3a), the carbon content of LLO@C&NiCo is 6.08 wt%. An obvious weight gain at 350 °C is due to the oxidization of NiCo alloy, which is supported by an exothermic peak from DSC curve. Two broad peaks in the Raman spectrum of LLO@C&NiCo (Fig. 3b) located at around 1349 and 1585 cm<sup>-1</sup> are assigned to the D (disorder-induced phonon mode) and G (graphite band) bands, respectively [46]. The intensity ratio of D band to G band ( $I_D/I_G$ ) is found to be 1.01, indicating the partly graphitized nature of the derived carbon shell. XPS measurement was performed to investigate the variation in valence state and composition (Fig. 3c–f). For LLO, the observed binding energies coincide well with Ni<sup>2+</sup>, Co<sup>3+</sup> and Mn<sup>4+</sup>, respectively [47,48]. After coating process, the binding energies for Mn 2p spectrum of LLO@C&NiCo are retained, indicating that the valence state of Mn is retained after carbonization; while the peaks of Ni 2p<sub>1/2</sub>, Ni 2p<sub>3/2</sub>, Co 2p<sub>1/2</sub> and Co 2p<sub>3/2</sub> slightly shift toward lower binding energies, suggesting that the lower nickel and cobalt oxidation states are appeared. The variations in Ni and Co oxidation are reasonably attributed to the existence of zero-valence NiCo alloy nanodots. Elemental mapping images (Fig. S7 online) confirm the homogeneous distribution

of Ni, Co, Mn, N and C in the particles, where the N and C originate from the derived carbon shell.

### 3.2. Electrochemical performance

The superiority of LLO@C&NiCo compared to LLO is revealed by electrochemical characterizations as a LIB cathode in the potential range of 2.0–4.8 V. The 1st, 5th, 10th, 25th and 50th charge-discharge voltage profiles at the current density of 0.2 C are shown in Fig. 4a, b. During the first charge process, both two samples exhibit two characteristic stages for Li-rich layered materials: a smoothly sloping voltage profile below 4.5 V and a long plateau around 4.5 V, together with a sloping region up to 4.8 V. The first discharge capacity of LLO@C&NiCo reaches 254 mAh g<sup>-1</sup>, which is higher than that of LLO (234 mAh g<sup>-1</sup>). The corresponding CV curves of LLO and LLO@C&NiCo are presented in Fig. S8 (online). According to the cycling performance at 0.4 C (Fig. 4c), LLO@C&NiCo electrode exhibits a high capacity and a stable cycling with the capacity retained at 270 mAh g<sup>-1</sup> after 100 cycles (capacity retention of 95%). In contrast, the capacity of LLO shows a slight increase in the initial state and then decreases to 192 mAh g<sup>-1</sup> after 100 cycles (capacity retention of 75%). The LLO@C&NiCo also exhibits a higher Coulombic efficiency of 72% at the initial cycle compared with that of LLO (66%). At the current density of 2 C (Fig. 4d), LLO@C&NiCo electrode also shows a higher discharge capacity and better stability (90% capacity retention after 300

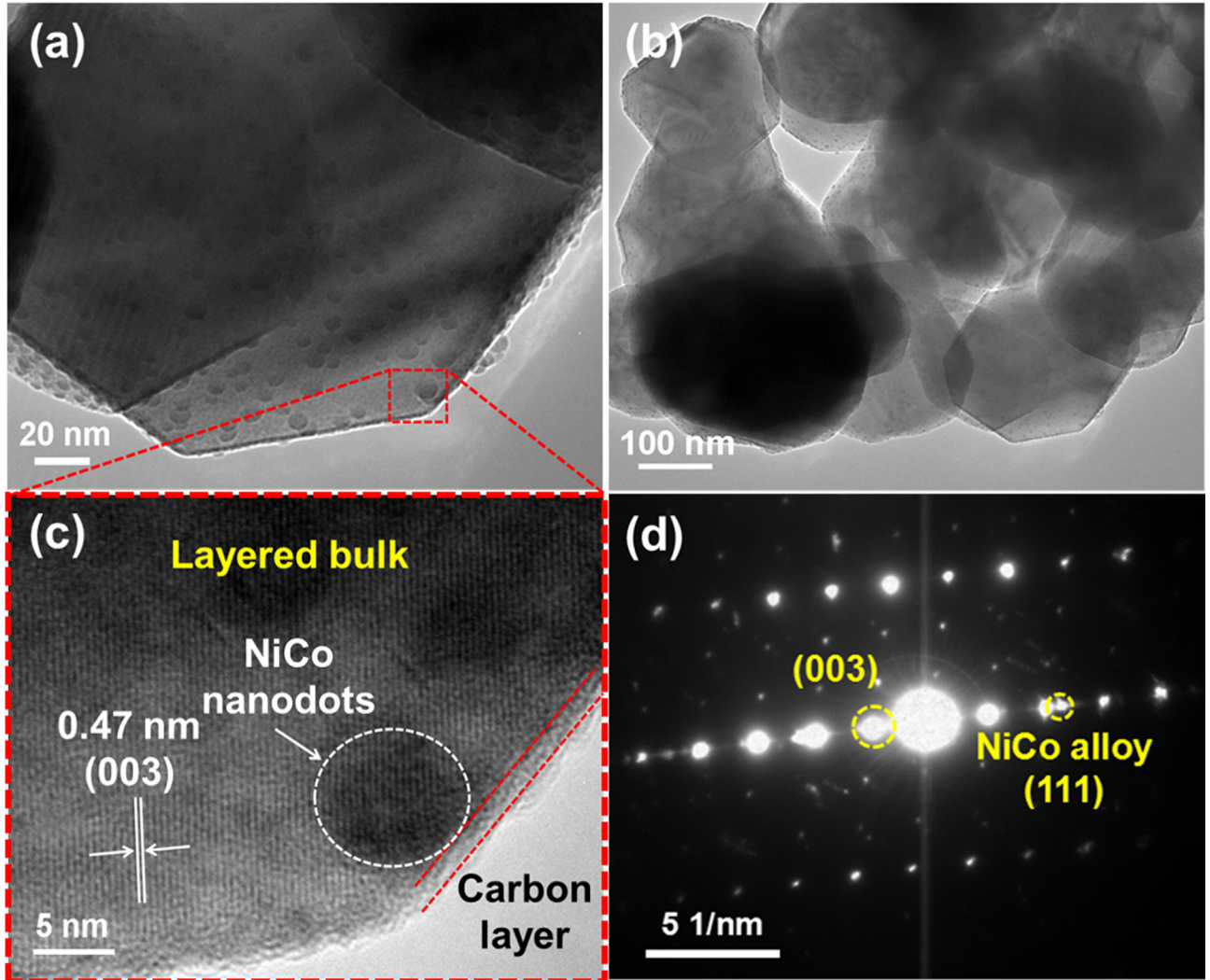


**Fig. 2.** (Color online) Electron microscopy characterizations of LLO@C&NiCo. (a), (b) TEM images, (c) HRTEM image and (d) SAED pattern.

cycles) than those of LLO (73%). Moreover, the LLO@C&NiCo electrode exhibits enhanced rate capability than LLO (Fig. 4e). The average specific discharge capacities are 289, 260, 235, 190 and 159 mAh g<sup>-1</sup> at 0.2, 0.5, 1, 2 and 5 C, respectively, while the corresponding capacities of LLO are 280, 235, 193, 150 and 105 mAh g<sup>-1</sup>. The capacity quickly recovers to as high as 287 mAh g<sup>-1</sup> when the current density is reduced back to 0.2 C, suggesting extraordinary stability of the LLO@C&NiCo. The corresponding charge-discharge voltage profiles of LLO and LLO@C&NiCo are shown in Fig. S9 (online). The EIS plots which were obtained at 4.5 V after 50 cycles at 0.4 C (Fig. 4f) indicate that the charge-transfer resistance and diffusion impedance of LLO@C&NiCo are smaller than those of LLO, implying fast electron and ion transport. Moreover, the conductivity is  $(4.5\text{--}5.5) \times 10^{-8}$  S cm<sup>-1</sup> for LLO@C&NiCo, ~5 times higher than that of LLO ( $(0.9\text{--}1.1) \times 10^{-8}$  S cm<sup>-1</sup>) (Fig. S10 online). The enhanced electrochemical performances of LLO@C&NiCo cathode are mainly attributed to the unique C&NiCo shell which endows the LLO@C&NiCo electrode with high electronic conductivity and robust structure.

### 3.3. Mechanism study

The crystal structure evolution of LLO and LLO@C&NiCo samples during the first two cycles were investigated through *in situ* XRD

technique (Fig. 5). For LLO@C&NiCo electrode, during the first charge process from open circuit voltage to 4.5 V, it is clear that the main (0 0 3) peak shifts to low angle. This phenomenon is attributed to the extraction of lithium ions from Li<sub>2</sub>MnO<sub>3</sub> phase and the increase of electrostatic repulsion between oxygen layers [49]. After charging to 4.8 V, the peak shifts to high angle; and then, when discharging to 3.8 V, the peak shifts towards low angle. These behaviors are caused by the extraction and insertion of lithium ions from LiMO<sub>2</sub> phase [49]. However, the (0 0 3) peak of LLO shifts dramatically accompanied by obvious widening (Fig. 5a-c) during this process, indicating that the LLO@C&NiCo has a better structural stability upon the Li<sup>+</sup> insertion/extraction processes. Finally, the peak re-shifts to high angle (down to 2.0 V) and returns to the original position. At this stage, the vacancies of the Li<sub>2</sub>MnO<sub>3</sub> phase in LLO@C&NiCo are filled with lithium ions, which decreases the electrostatic repulsion between oxygen layers [49]. The shift behavior during the second cycle is similar to that in the first cycle, but the intensity of (0 0 3) peak for LLO dramatically decreases.

The SEM images (Fig. 6a, e) after 50 cycles at 0.4 C show that the original shape of LLO@C&NiCo is well preserved while the structure of LLO exhibits serious damage. According to the HRTEM images of LLO after 50 cycles at 0.4 C, the amorphous phase is generated in the interior of the grains, and the initial monocrystalline

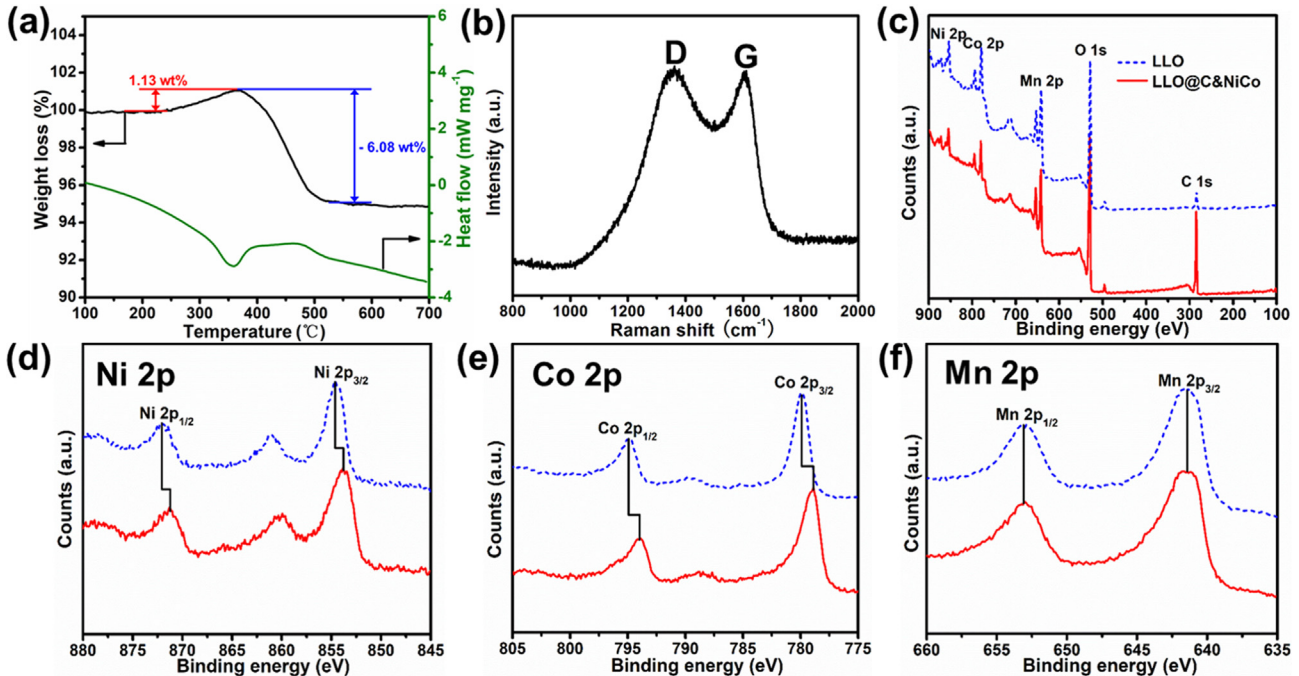


**Fig. 3.** (Color online) Characterizations of the C&NiCo shell. (a) TG and DSC curves of LLO@C&NiCo in air at  $10\text{ }^{\circ}\text{C min}^{-1}$ ; (b) Raman spectrum of LLO@C&NiCo; (c)–(f) XPS survey spectra and the corresponding spectra of Ni 2p, Co 2p and Mn 2p, respectively for LLO and LLO@C&NiCo.

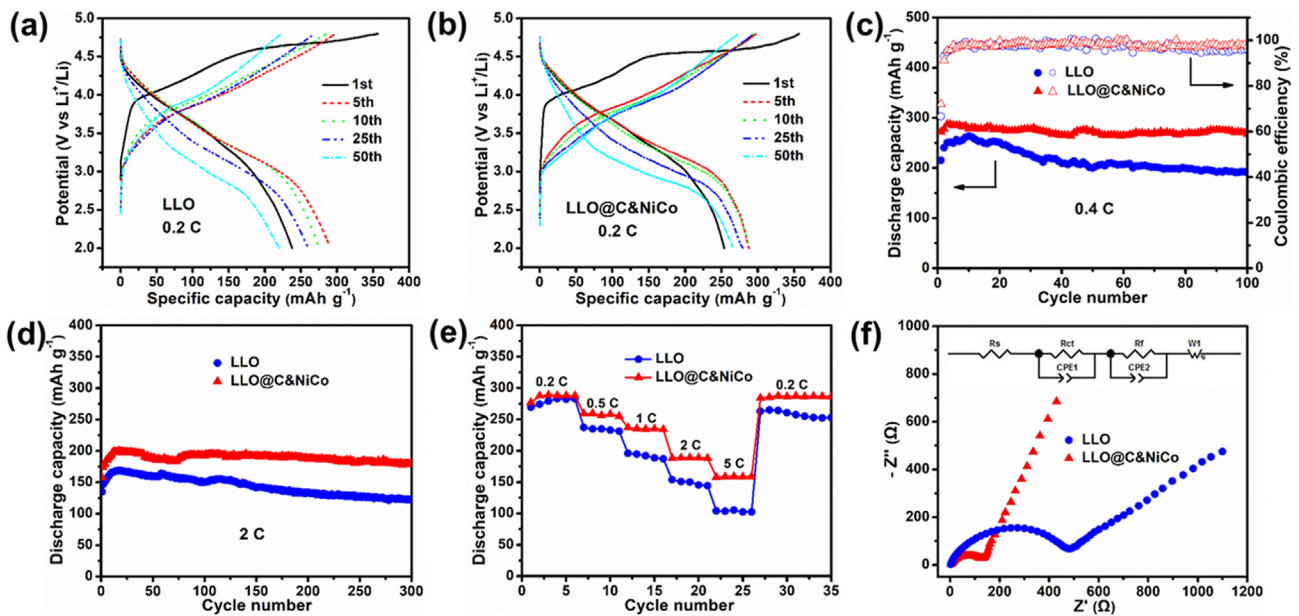


**Fig. 4.** (Color online) Electrochemical performances of LLO and LLO@C&NiCo samples in the potential range of 2.0–4.8 V. Charge-discharge curves (for the 1st, 5th, 10th, 25th and 50th cycle at the rate of 0.2 C) of LLO (a) and LLO@C&NiCo (b); Cycling performance and the corresponding Coulombic efficiencies tested at current densities of 0.4 (c) and 2 C (d); (e) Rate performance conducted at current densities of 0.2, 0.5, 1, 2, and 5 C; (f) Nyquist plots measured at the same equilibrium potential in the frequency range of 100 kHz–0.01 Hz.

is transformed into polycrystalline LLO (Fig. 6b, c). In contrast, the initial monocrystalline and NiCo nanodots of LLO@C&NiCo are well preserved after cycling (Fig. 6f, g). Further, the corresponding SAED pattern also reveals the polycrystalline nature of LLO, with two diffraction rings indexed to (4 0 0) and (4 4 0) crystal planes of spinel phase (Fig. 6d) [50], while the hexagonal symmetry structure of LLO@C&NiCo is well preserved (Fig. 6h). This result indicates that the undesired formation of the spinel phase initiated from the par-

ticle surface during cycling is efficiently suppressed for LLO@C&NiCo.

LLO@C&NiCo as a cathode material for LIBs exhibiting superior electrochemical performances compared with some previous reports (Table S1 online), is due to its unique protective C&NiCo shell. It allows fast electron and ion transport, provides a robust structure for LLO which suppresses the undesired formation of the spinel phase initiated from the particle surface during cycling,

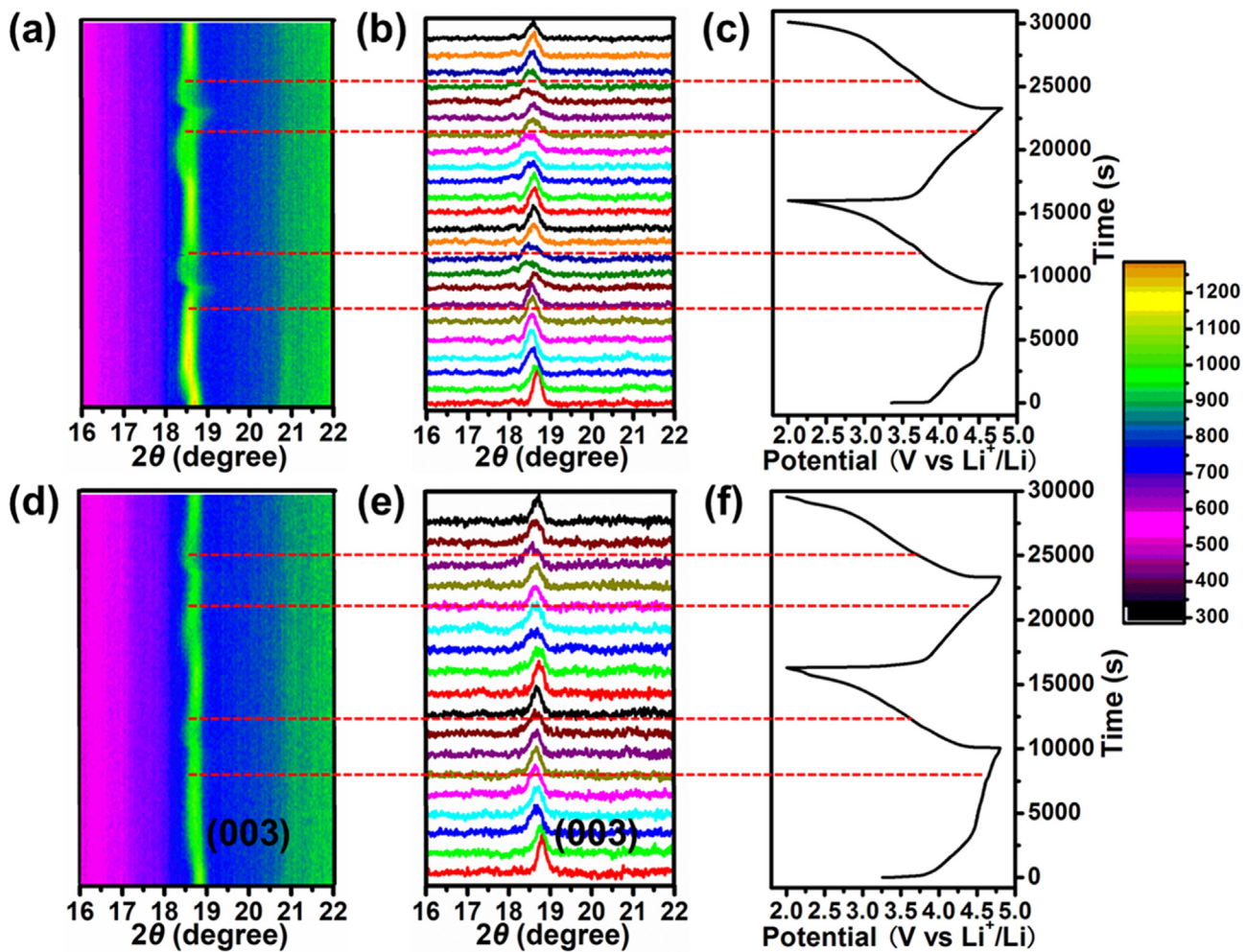


**Fig. 5.** (Color online) *In situ* XRD characterization of LLO (a)–(c) and LLO@C&NiCo (d)–(f).

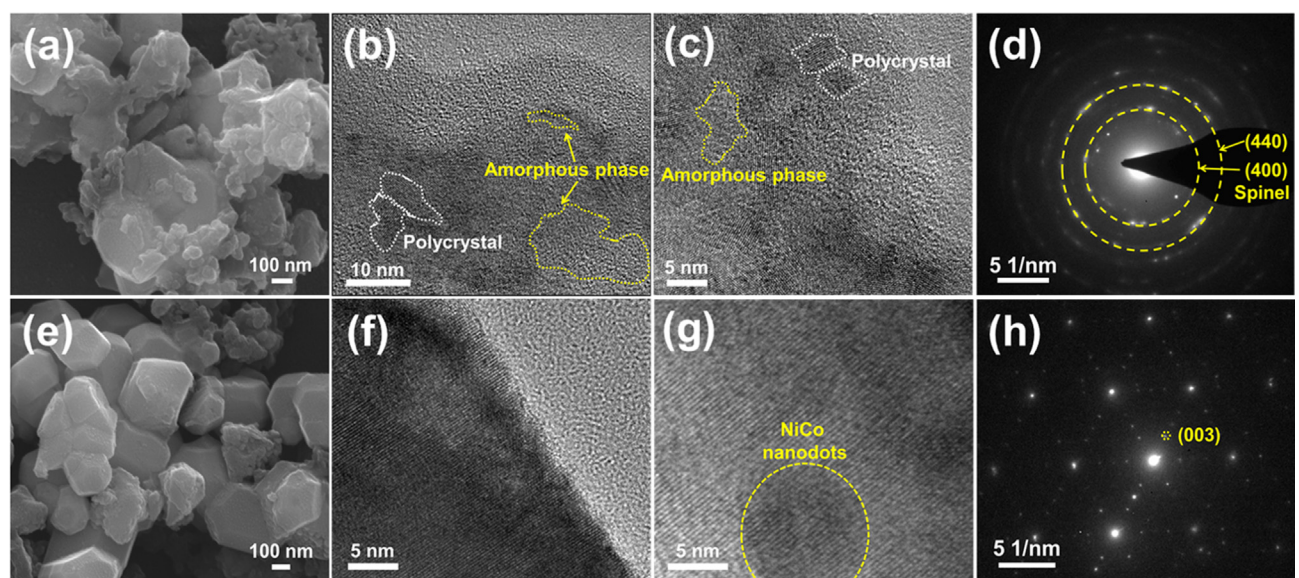


**Fig. 6.** (Color online). Electron microscopy characterizations of electrode materials after 50 cycles at 0.4 C. SEM, HRTEM images and SAED patterns of LLO (a)–(d) and LLO@C&NiCo (e)–(h).

and protects the surface structure from side reactions at the electrode/electrolyte interface.

#### 4. Conclusion

A facile and novel MOF shell-derived surface modification strategy has been developed to synthesize NiCo nanodots decorated carbon-confined  $\text{Li}_{1.2}\text{Mn}_{0.54}\text{Ni}_{0.13}\text{Co}_{0.13}\text{O}_2$  nanoparticles via low-pressure vapor superassembly and subsequent controlled pyrolysis. As a proof-of-concept application, the obtained LLO@C&NiCo cathode exhibits enhanced performance as the LIB cathode compared to LLO, with a capacity retention of 95% after 100 cycles at 0.4 C and a high capacity of 159 mAh g<sup>-1</sup> at 5 C. The enhanced electrochemical performances of LLO@C&NiCo cathode are mainly attributed to the unique C&NiCo shell, which endows the inner LLO with high electronic conductivity and robust structure. The presented work may provide a new insight into the design and synthesis of high-performance electrode materials and further pave the path for the next-generation high performance LIBs.

#### Conflict of interest

The authors declare that they have no conflict of interest.

#### Acknowledgments

This work was supported by the National Key Research and Development Program of China (2016YFA0202603), the National Basic Research Program of China (2013CB934103), the Programme of Introducing Talents of Discipline to Universities (B17034), the National Natural Science Foundation of China (51521001), the National Natural Science Fund for Distinguished Young Scholars (51425204), and the Fundamental Research Funds for the Central Universities (WUT: 2016III001 and 2016-YB-004). Prof. Liqiang Mai gratefully acknowledged financial support from China Scholarship Council (201606955096).

#### Appendix A. Supplementary data

Supplementary data associated with this article can be found, in the online version, at <https://doi.org/10.1016/j.scib.2017.12.011>.

#### References

- [1] Mai L, Yan M, Zhao Y. Track batteries degrading in real time. *Nature* 2017;546:469–70.
- [2] Meng J, Guo H, Niu C, et al. Advances in structure and property optimizations of battery electrode materials. *Joule* 2017;1:522–47.
- [3] Wang L, Hu Z, Zhao K, et al. Hollow spherical  $\text{LiNi}_{0.5}\text{Mn}_{1.5}\text{O}_4$  built from polyhedra with high-rate performance via carbon nanotube modification. *Sci China Mater* 2016;59:95–103.
- [4] Meng J, Niu C, Xu L, et al. General oriented formation of carbon nanotubes from metal-organic frameworks. *J Am Chem Soc* 2017;139:8212–21.
- [5] Chan CK, Peng H, Liu G, et al. High-performance lithium battery anodes using silicon nanowires. *Nat Nanotechnol* 2008;3:187–91.
- [6] Konarov A, Myung ST, Sun YK. Cathode materials for future electric vehicles and energy storage systems. *ACS Energy Lett* 2017;2:703–8.
- [7] Thackeray MM, Wolverton C, Isaacs ED. Electrical energy storage for transportation—approaching the limits of, and going beyond, lithium-ion batteries. *Energy Environ Sci* 2012;5:7854–63.
- [8] Thackeray MM, Kang SH, Johnson CS, et al.  $\text{Li}_2\text{MnO}_3$ -stabilized  $\text{LiMO}_2$  ( $M = \text{Mn}, \text{Ni}, \text{Co}$ ) electrodes for lithium-ion batteries. *J Mater Chem* 2007;17:3112–25.
- [9] Choi NS, Chen Z, Freunberger SA, et al. Challenges facing lithium batteries and electrical double-layer capacitors. *Angew Chem Int Ed* 2012;51:9994–10024.
- [10] Yu H, Zhou H. High-energy cathode materials ( $\text{Li}_2\text{MnO}_3$ – $\text{LiMO}_2$ ) for lithium-ion batteries. *J Phys Chem Lett* 2013;4:1268–80.
- [11] Robert R, Villevieille C, Novák P. Enhancement of the high potential specific charge in layered electrode materials for lithium-ion batteries. *J Mater Chem A* 2014;2:8589–98.
- [12] Xia Q, Zhao X, Xu M, et al. A Li-rich layered@spinel@carbon heterostructured cathode material for high capacity and high rate lithium-ion batteries fabricated via an *in situ* synchronous carbonization-reduction method. *J Mater Chem A* 2015;3:3995–4003.
- [13] Xu H, Deng S, Chen G. Improved electrochemical performance of  $\text{Li}_{1.2}\text{Mn}_{0.54}\text{Ni}_{0.13}\text{Co}_{0.13}\text{O}_2$  by Mg doping for lithium ion battery cathode material. *J Mater Chem A* 2014;2:15015–21.
- [14] Zhang H, Qiao Q, Li G, et al.  $\text{PO}_4^{3-}$  polyanion-doping for stabilizing Li-rich layered oxides as cathode materials for advanced lithium-ion batteries. *J Mater Chem A* 2014;2:7454–60.
- [15] Zhao T, Chen S, Li L, et al. Synthesis, characterization, and electrochemistry of cathode material  $\text{Li}[\text{Li}_{0.2}\text{Co}_{0.13}\text{Ni}_{0.13}\text{Mn}_{0.54}]_{\text{O}_2}$  using organic chelating agents for lithium-ion batteries. *J Power Sources* 2013;228:206–13.
- [16] Li L, Zhang X, Chen R, et al. Synthesis and electrochemical performance of cathode material  $\text{Li}_{1.2}\text{Co}_{0.13}\text{Ni}_{0.13}\text{Mn}_{0.54}\text{O}_2$ , from spent lithium-ion batteries. *J Power Sources* 2014;249:28–34.
- [17] Zhao Y, Liu J, Wang S, et al. Surface structural transition induced by gradient polyanion-doping in Li-rich layered oxides: implications for enhanced electrochemical performance. *Adv Funct Mater* 2016;26:4760–7.
- [18] Wei W, Chen L, Pan A, et al. Roles of surface structure and chemistry on electrochemical processes in lithium-rich layered oxide cathodes. *Nano Energy* 2016;30:580–602.
- [19] Lu Z, Dahn JR. Understanding the anomalous capacity of  $\text{Li}/[\text{Li}_{x}\text{Li}_{(1/3-2x)/3}\text{Mn}_{(2/3-x)/3}]_{\text{O}_2}$  cells using *in situ* X-ray diffraction and electrochemical studies. *J Electrochem Soc* 2002;149:A815–22.
- [20] Armstrong AR, Holzapfel M, Novák P, et al. Demonstrating oxygen loss and associated structural reorganization in the lithium battery cathode  $\text{Li}[\text{Ni}_{0.2}\text{Li}_{0.2}\text{Mn}_{0.6}]_{\text{O}_2}$ . *J Am Chem Soc* 2006;128:8694–8.
- [21] Hong YS, Park YJ, Ryu KS, et al. Synthesis and electrochemical properties of nanocrystalline  $\text{Li}[\text{Ni}_{x}\text{Li}_{(1-2x)/3}\text{Mn}_{(2-x)/3}]_{\text{O}_2}$  prepared by a simple combustion method. *J Mater Chem* 2004;14:1424–9.
- [22] Sathiya M, Ramesha K, Rousse G, et al. High performance  $\text{Li}_2\text{Ru}_{1-y}\text{Mn}_y\text{O}_3$  ( $0.2 \leq y \leq 0.8$ ) cathode materials for rechargeable lithium-ion batteries: their understanding. *Chem Mater* 2013;25:1121–31.
- [23] Gu M, Belharouak I, Zheng J, et al. Formation of the spinel phase in the layered composite cathode used in Li-ion batteries. *ACS Nano* 2013;7:760–7.
- [24] Xu B, Fell CR, Chi M, et al. Identifying surface structural changes in layered Li-excess nickel manganese oxides in high voltage lithium ion batteries: a joint experimental and theoretical study. *Energy Environ Sci* 2011;4:2223–33.
- [25] Mohanty D, Sefat AS, Kalnaus S, et al. Investigating phase transformation in the  $\text{Li}_{1.2}\text{Co}_{0.1}\text{Mn}_{0.55}\text{Ni}_{0.15}\text{O}_2$  lithium-ion battery cathode during high-voltage hold (4.5 V) via magnetic, X-ray diffraction and electron microscopy studies. *J Mater Chem A* 2013(1):6249–61.
- [26] Zheng J, Gu M, Xiao J, et al. Corrosion/fragmentation of layered composite cathode and related capacity/voltage fading during cycling process. *Nano Lett* 2013;13:3824–30.
- [27] Nayak PK, Grinblat J, Levi M, et al. Al doping for mitigating the capacity fading and voltage decay of layered Li and Mn-rich cathodes for Li-ion batteries. *Adv Energy Mater* 2016;6:1502398.
- [28] Li L, Song B, Chang Y, et al. Retarded phase transition by fluorine doping in Li-rich layered  $\text{Li}_{1.2}\text{Mn}_{0.54}\text{Ni}_{0.13}\text{Co}_{0.13}\text{O}_2$  cathode material. *J Power Sources* 2015;283:162–70.
- [29] Li B, Yan H, Ma J, et al. Manipulating the electronic structure of Li-rich manganese-based oxide using polyanions: towards better electrochemical performance. *Adv Funct Mater* 2014;24:5112–8.
- [30] Li G, Feng X, Ding Y, et al.  $\text{AlF}_3$ -coated  $\text{Li}(\text{Li}_{0.17}\text{Ni}_{0.25}\text{Mn}_{0.58})_{\text{O}_2}$  as cathode material for Li-ion batteries. *Electrochim Acta* 2012;78:308–15.
- [31] Kobayashi G, Irii Y, Matsumoto F, et al. Improving cycling performance of Li-rich layered cathode materials through combination of  $\text{Al}_2\text{O}_3$ -based surface modification and stepwise precycling. *J Power Sources* 2016;303:250–6.
- [32] Wu Y, Vadivel Murugan A, Manthiram A. Surface modification of high capacity layered  $\text{Li}[\text{Li}_{0.2}\text{Mn}_{0.54}\text{Ni}_{0.13}\text{Co}_{0.13}]_{\text{O}_2}$  cathodes by  $\text{AlPO}_4$ . *J Electrochem Soc* 2008;155:A635–41.
- [33] Zhang J, Zhang H, Gao R, et al. New insights into the modification mechanism of Li-rich  $\text{Li}_{1.2}\text{Mn}_{0.6}\text{Ni}_{0.2}\text{O}_2$  coated by  $\text{Li}_2\text{ZrO}_3$ . *Phys Chem Chem Phys* 2016;18:13322–31.
- [34] Liu B, Zhang Q, He S, et al. Improved electrochemical properties of  $\text{Li}_{1.2}\text{Ni}_{0.18}\text{Mn}_{0.59}\text{Co}_{0.03}\text{O}_2$  by surface modification with  $\text{LiCoPO}_4$ . *Electrochim Acta* 2011;56:6748–51.
- [35] Zheng F, Yang C, Xiong X, et al. Nanoscale surface modification of lithium-rich layered-oxide composite cathodes for suppressing voltage fade. *Angew Chem Int Ed* 2015;54:13058–62.
- [36] Wang J, Sun X. Understanding and recent development of carbon coating on  $\text{LiFePO}_4$  cathode materials for lithium-ion batteries. *Energy Environ Sci* 2012;5:5163–85.
- [37] Lee S, Cho Y, Song H, et al. Carbon-coated single-crystal  $\text{LiMn}_2\text{O}_4$  nanoparticle clusters as cathode material for high-energy and high-power lithium-ion batteries. *Angew Chem Int Ed* 2012;51:8748–52.
- [38] Kim HS, Kong M, Kim K, et al. Effect of carbon coating on  $\text{LiNi}_{1/3}\text{Mn}_{1/3}\text{Co}_{1/3}\text{O}_2$  cathode material for lithium secondary batteries. *J Power Sources* 2007;171:917–21.
- [39] Xu J, Jia G, Mai W, et al. Energy storage performance enhancement by surface engineering of electrode materials. *Adv Mater Interfaces* 2016;3:1600430.
- [40] Meng J, Liu X, Li J, et al. General oriented synthesis of precise carbon-confined nanostructures by low-pressure vapor superassembly and controlled pyrolysis. *Nano Lett* 2017. <https://doi.org/10.1021/acs.nanolett.7b03982>.

- [41] Li Q, Li G, Fu C, et al. Balancing stability and specific energy in Li-rich cathodes for lithium ion batteries: a case study of a novel Li-Mn-Ni-Co oxide. *J Mater Chem A* 2015;3:10592–602.
- [42] Feng X, Yang Z, Tang D, et al. Performance improvement of Li-rich layer-structured  $\text{Li}_{1.2}\text{Mn}_{0.54}\text{Ni}_{0.13}\text{Co}_{0.13}\text{O}_2$  by integration with spinel  $\text{LiNi}_{0.5}\text{Mn}_{1.5}\text{O}_4$ . *Phys Chem Chem Phys* 2015;17:1257–64.
- [43] Ma J, Li B, Li A, et al. A highly homogeneous nanocoating strategy for Li-rich Mn-based layered oxides based on chemical conversion. *J Power Sources* 2015;277:393–402.
- [44] Yang J, Zhang F, Lu H, et al. Hollow Zn/Co ZIF particles derived from core-shell ZIF-67@ZIF-8 as selective catalyst for the semi-hydrogenation of acetylene. *Angew Chem Int Ed* 2015;54:10889–93.
- [45] Poizot P, Laruelle S, Gruegeon S, et al. Nano-sized transition-metal oxides as negative-electrode materials for lithium-ion batteries. *Nature* 2000;407:496–9.
- [46] He Q, Liu J, Li Z, et al. Solvent-free synthesis of uniform MOF shell-derived carbon confined  $\text{SnO}_2/\text{Co}$  nanocubes for highly reversible lithium storage. *Small* 2017;1701504.
- [47] Zhang X, Belharouak I, Li L, et al. Structural and electrochemical study of  $\text{Al}_2\text{O}_3$  and  $\text{TiO}_2$  coated  $\text{Li}_{1.2}\text{Mn}_{0.54}\text{Ni}_{0.13}\text{Co}_{0.13}\text{O}_2$  cathode material using ALD. *Adv Energy Mater* 2013(3):1299–307.
- [48] Fu Q, Du F, Bian X, et al. Electrochemical performance and thermal stability of  $\text{Li}_{1.18}\text{Co}_{0.15}\text{Ni}_{0.15}\text{Mn}_{0.52}\text{O}_2$  surface coated with the ionic conductor  $\text{Li}_3\text{VO}_4$ . *J Mater Chem A* 2014(2):7555–62.
- [49] Mohanty D, Kalnaus S, Meissner RA, et al. Structural transformation of a lithium-rich  $\text{Li}_{1.2}\text{Co}_{0.1}\text{Mn}_{0.55}\text{Ni}_{0.15}\text{O}_2$  cathode during high voltage cycling resolved by *in situ* X-ray diffraction. *J Power Sources* 2013;229:239–48.
- [50] Kohli S, Mccurdy PR, Johnson DC, et al. Template-assisted chemical vapor deposited spinel ferrite nanotubes. *J Mater Chem C* 2010;114:19557–61.